Environmental Science and Pollution Research (2023) 30:63535–63548
https://doi.org/10.1007/s11356-023-26896-4

RESEARCH ARTICLE

Preparation and evaluation of celite decorated iron nanoparticles for the sequestration performance of hexavalent chromium from aqueous solution

Xiankui Cheng[1] · Junjie Chen[1] · Hui Li[2] · Guodong Sheng[1]

Received: 16 February 2023 / Accepted: 4 April 2023 / Published online: 13 April 2023

Abstract

The increasing usage of an important heavy metal chromium for industrial purposes, such as metallurgy, electroplating, leather tanning, and other fields, has contributed to an augmented level of hexavalent chromium (Cr(VI)) in watercourses negatively impacting the ecosystems and significantly making Cr(VI) pollution a serious environmental issue. In this regard, iron nanoparticles exhibited great reactivity in remediation of Cr(VI)-polluted waters and soils, but, the persistence and dispersion of the raw iron should be improved. Herein, this article utilized an environment-friendly celite as a modifying reagent and described the preparation of a novel composites namaly celite decorated iron nanoparticles (C-Fe^0) and evaluation of C-Fe^0 for the sequestration performance of Cr(VI) from aqueous solution. The results indicated that initial Cr(VI) concentration, adsorbent dosage, and especially solution pH are all critical factors to control C-Fe^0 performance in Cr(VI) sequestration. We demonstrated that C-Fe^0 could achieve a high Cr(VI) sequestration efficiency with an optimized adsorbent dosage. Fitness of the pseudo-second-order kinetics model with data indicated that adsorption was the rate-controlling step and chemical interaction controlled Cr(VI) sequestration on C-Fe^0. The adsorption isotherm of Cr(VI) could be the best depicted by Langmuir model with a monolayer adsorption. The underlying sequestration path of Cr(VI) by C-Fe^0 was then put forward, and the combined effect of adsorption and reduction implied the potentials of C-Fe^0 in Cr(VI) removal.

Keywords Cr(VI) · Iron nanoparticles · Celite · Sequestration

Introduction

With the fast advancement of industrial civilization worldwide, as well as the rapid global economic development, a large number of contaminants of metal(loid)s have been widely detected in the natural soil and water bodies (Fan et al. 2023; Gu et al. 2022; Hao et al. 2023; Li et al. 2021a; Ling et al. 2017). These contaminants of metal(loid) ion, which mainly included U(VI) (Bone et al. 2017; Hu et al. 2020; Kou et al. 2022; Pan et al. 2023), Se(IV)/Se(VI) (Hong et al. 2020; Kou et al. 2022; Lu et al. 2018; Wu et al. 2021), Cr(VI) (Lu et al. 2018; Wu et al. 2021), Mo(VI) (Li et al. 2020), Re(VII) (Li et al. 2020), ^{99}Tc(VII) (Boglaienko et al. 2019), Eu(III) (Dong et al. 2018, 2021), Co(II) (Xing et al. 2016), As(III)/As(V) (Wang et al. 2014), Pb(II) (Zhao et al. 2018), Cd(II) (Awual et al. 2018; Zhao et al. 2018), Ni(II) (Flynn and Catalano 2017), rare earth (Li et al. 2021b), and so on, have been commonly reported to pose severe threats to aquatic ecosystems and human health even at trace levels due to their great toxic effects and have been increasingly becoming an ecological concern (Fan et al. 2023; Ling et al. 2017). So, their decontamination from various soil and water bodies has been an important and constant concern. In this respect, a variety of treatment approaches which included adsorption, coagulation, chemical, and biological treatment have been developed to remove metal(loid)s from water (Wan et al. 2018).

Among these metal(loid)s as-mentioned above, chromium (Cr) is one of the most common contaminants that could be

Responsible Editor: George Z. Kyzas

✉ Guodong Sheng
gdsheng@usx.edu.cn

[1] School of Chemistry and Chemical Engineering, Zhejiang Engineering Research Center of Fat-Soluble Vitamin, Shaoxing University, Zhejiang 312000, People's Republic of China

[2] School of Medicine, Shaoxing University, Shaoxing, Zhejiang 312000, People's Republic of China

found in the hazardous waste sites, often entering groundwater and soil environment from industrial effluents (Fan et al. 2023; Ling et al. 2017; Liu et al. 2023). Because of its high physiological toxicity, Cr has been regarded as a priority contaminant and environmental hazard, and thus it is very imperative to secure an effective method for the quick and complete removal of Cr from contaminated ecological environment (Ling et al. 2017). For Cr in the natural environment, there are two major oxidation states namely Cr(III) that is slightly soluble and considerably less toxic, as well as Cr(VI) that is more toxic, soluble, and mobile (Chen et al. 2021; Kang et al. 2020; Li et al. 2016, 2022; Saslow et al. 2018; Wu et al. 2020). These are three reasons for the fact that Cr(VI) is more toxic than Cr(III). First, Cr(VI) is labile but Cr(III) is inert. Then, Cr(VI) enters the cell via sulfate uptake pathway because of structural similarity of chromate with sulfate but Cr(III) cannot. Finally, Cr(VI) is mobile but Cr(III) is not (Saha et al. 2013a, b). Besides, Cr(VI) could enter into the natural environment via different sources (Saha and Orvig 2010; Saha et al. 2011). Thereby it is more important to find an effective and convenient method to control Cr(VI) exposure and reduce its toxic effect, and reduction of Cr(VI) into Cr(III) by biological material has been regarded as a very useful and cheap process (Mukherjee et al. 2014, 2015a, b, 2016; Nandi et al. 2017; Saha and Saha 2014). Using a high-performance photocatalyst for the efficient photocatalytic reduction of aqueous Cr (VI) into Cr(III) was also reported to be an important method (Ge et al. 2021; Yao et al. 2022a, b; Zhang et al. 2014, 2018, 2022). Besides, lots of other materials have been fabricated for reduction of Cr(VI) into Cr(III) from water bodies including iron carbide loaded on the N-doped carbon nanotubes, the FeS and titanate nanotubes nanocomposites, the graphene oxide adsorbed Fe(II), the h-BN supported nanoscale iron sulfide composite, etc. (Chen et al. 2021; Kang et al. 2020; Li et al. 2016, 2022; Liu et al. 2023; Saslow et al. 2018; Wu et al. 2020).

Among these materials and Cr(VI) remediation systems as-mentioned above, utilizing iron (Fe^0) nanoparticles and their nanocomposites has been generally regarded as one of the most promising methods for the remediation of Cr(VI) and other related metal(loid)s from contaminated soil and water as a result of their high specific surface area and high reactive surface sites (Chen et al. 2017, 2023; Gu et al. 2007; Li et al. 2010; Shi et al. 2011a, b; Soliemanzadeh and Fekri 2017; Wei et al. 2021; Zhang et al. 2013). Besides, iron nanoparticles and their nanocomposites were also considered a reactive material in permeable reactive barriers (PRBs), which could provide enormous flexibility for both in situ and ex situ remediation applications of metal(loid)s (Li et al. 2010). So, considerable research on Cr(VI) remediation has been focused on the interaction kinetics and reaction mechanisms between Fe^0-based materials and Cr(VI). The remediation of Cr(VI) in Fe^0-based interaction systems was mainly ascribed to a procedure that involved the reductive precipitation of Cr(VI) into Cr(III), which was resulted from an electron transfer interaction between Cr(VI) and Fe(0)/Fe(II) at a solid/water interface (Shi et al. 2011a, b; Soliemanzadeh and Fekri 2017; Zhang et al. 2013). In addition, during the potential applications, decorated iron nanoparticles could be improved in the dispersion and persistence of iron nanoparticles in water, and thus enhancing the speed and efficiency of a Fe^0-based remediation system. In this regard, clay minerals, which are environmental-friendly and abundant in nature, are promising modifying reagent, and therefore lots of clay minerals like bentonite and montmorillonite have been widely utilized to decorate iron nanoparticles (Shi et al. 2011a, b; Soliemanzadeh and Fekri 2017; Zhang et al. 2013). As an inert and porous material, celite was mainly composed of silica (SiO_2), as well as some other inorganic oxides (Abbasi et al. 2023; Chang et al. 2007; Jabli et al. 2020; Liu et al. 2009; Meunier et al. 2014; Satar and Husain 2009). Since celite has desirable physical properties, i.e., inexpensive, chemical inertness, non-biodegradable, as well as interconnected pore structure, celite is very suitable for support of reactive materials. Thereby, there is a growing interest in the utilization of celite as support material of the catalyst by providing a better distribution to enhance reaction rates (Abbasi et al. 2023; Chang et al. 2007; Jabli et al. 2020; Liu et al. 2009; Meunier et al. 2014; Satar and Husain 2009). Nevertheless, according to our literature survey, no attention has been paid to the usage of celite as a modifying reagent to decorate iron (Fe^0) nanoparticles.

Therefore, in the present paper, we aimed to prepare celite decorated iron nanoparticles (C-Fe^0) and evaluate the sequestration performance of hexavalent chromium by C-Fe^0 from aqueous solution. The main objectives of this paper were: (1) to prepare celite decorated iron nanoparticles and characterize the surface structure and properties using scanning electron microscopy (SEM), transmission electron microscopy (TEM), Fourier transform infrared (FTIR) spectra, X-ray diffraction (XRD), etc., (2) to investigate the adsorption kinetics and isotherms of Cr(VI) on C-Fe^0 material, and (3) to reveal the interaction mechanisms between C-Fe^0 and Cr(VI) using X-ray photoelectron spectroscopy (XPS).

Materials and methods

Chemicals and equipment

All chemicals including potassium dichromate (Shanghai Zhanyun Chemical Co. LTD), diphenylarbazone (Shanghai Maclin Biochemical Technology Co., LTD), sulfamic acid (Shanghai Maclin Biochemical Technology Co., LTD), ferrous sulfate heptahydrate (Sinopharm Chemical Reagent

Co. LTD), phosphoric acid (Shanghai Zhanyun Chemical Co. LTD), sodium hydroxide (Xilong Chemical Co., LTD, hydrochloric acid (Zhejiang Zhongxing Chemical Reagent Co. LTD), sulfuric acid (Hangzhou Shuanglin Chemical Reagent Co. LTD), acetone (Hangzhou Shuanglin Chemical Reagent Co. LTD) were purchased in analytical purity without further treatment. The equipment used in this work included electronic analytical balance (EL204, Mettler Toledo (Shanghai) Instrument Co., LTD), precision pH meter (Five Easy Plus, Mettler Toledo (Shanghai) Instrument Co., LTD), CNC ultrasonic cleaner (KQ5200DA, Kunshan Ultrasonic Instrument Co., LTD), ultraviolet–visible spectrophotometer (SP-756-P, Shanghai Spectrometer Co. LTD), constant temperature heating magnetic agitator (DF-101S, Gongyi Yuhua Instrument Co., LTD), electric blast drying oven (GZX-9070MBE, Shanghai Boxun Industrial Co., LTD. Medical equipment factory), table top high speed centrifuge (TG16-WS, Hunan Xiangyi Laboratory Instrument Development Co., LTD), temperature controlled shaker(IKA KS4000i control, German aika), etc.

Experimental methods

To prepare celite decorated iron nanoparticles (C-Fe^0), first, a certain amount of celite was put in a 500-mL flask, then 250 mL of deoxidized deionized water was added, with constant stirring under nitrogen conditions to ensure deoxidization. After that, a certain amount of $FeSO_4{\cdot}7H_2O$ was added, and a peristaltic pump was used to add 50 mL of $NaBH_4$ solution at a rate of 4 mL/min (the molar ratio of $NaBH_4$ to Fe^{2+} is ~ 3:1). The reaction is as: $Fe^{2+} + 6H_2O + 2BH^-_4 \rightarrow Fe^0\downarrow + 2B(OH)_3 + 7H_2\uparrow$ (Liu et al. 2014; Shi et al. 2011a, b). During the reaction, nitrogen was always introduced for deoxidation, and after the adding completion of $NaBH_4$ solution, the stirring is continued for another 15 min, and thus the generated H_2 could be completely discharged. The as-prepared material was centrifuged and washed to remove impurity ions, then freeze-dried, and finally vacuum freeze-dried to obtain powdered C-Fe^0 material.

To evaluate the sequestration performance of Cr(VI) by C-Fe^0 from aqueous solution,the batch adsorption experiment was used, wherein the solutions of Cr(VI) with different concentrations are diluted by the stock solution, and these solutions were added in a certain volume of reaction bottles, then the pH of the reaction solution was adjusted with 0.1 mol/L of NaOH or 0.1 mol/L of HCl. Sodium salt (Na) was used for the adsorption studies. In order to obtain an optimization conditions for the adsorption of Cr(VI), the effects of adsorbent dosage, initial pH value of solution, initial concentration of Cr(VI), and contact time on the adsorption process were studied respectively. After shaking for a certain time with a rotating speed of 220 r/min, a certain volume of reaction filtrate was diluted in a 25-mL colorimetric tube to determine the concentration of Cr(VI) by spectrophotometry method (Liu et al. 2014; Shi et al. 2011a, b).

Determination methods

The surface morphology was observed with a JEOL, JSM-6360LV scanning electron microscope (SEM) and transmission electron microscope (TEM, JEO, JEM-1011). The elemental composition of the reaction samples was characterized by energy-dispersive X-ray spectroscopy (EDS, Oxford instruments X-Max). The phase analysis was determined by the powder X-ray diffraction (XRD) measurements (PANalytical B.V., Empyrean, NL). The Fourier transform infrared (FTIR) spectra were measured on a Nicolet 6700 FTIR spectrometric analyzer using KBr pellets. Surface electronic states were analyzed by X-ray photoelectron spectroscopy (XPS, ESCALAB 250xi of SEMER Fisher Scientific and Technological Co., Ltd), with a Ka-Al radiation (hv = 1486.6 eV). XPS spectra were analyzed by XPS peak fitting program for WIN95/98 (XPSPEAK 4.0 Version 4.1) using the following asymmetric Gaussian–Lorentzian sum function. Line shapes of GL (30) were used for individual constituents (i.e., O1s, Fe2p, and Cr2p) (Chen et al. 2022, 2023; Li et al. 2021a; Wu et al. 2021).

Results and discussion

Batch adsorption results

Figure 1 displayed the experimental results of the sequestration performance of Cr(VI) by C-Fe^0 via an adsorption process from aqueous solution as a function of solution pH, adsorbent dosage, and contact time. The optimization of pH played an important role in Cr(VI) adsorption on C-Fe^0 due to the direct determination of the species of Cr(VI) and surface charge of C-Fe^0 in water by the initial pH value. Previous studies have showed that Cr(VI) was mainly existed in the form of $HCrO_4^-$ at low pH values and CrO_4^{2-} was in a dominant position with pH increasing (Su et al. 2020). The effect of pH on sequestration performance of Cr(VI) by C-Fe^0 was presented in Fig. 1A. The efficiency of Cr(VI) sequestration slightly increased with pH increased from 2 to 3 and then obviously decreased with pH increasing from 3 to 8. This was mainly because the corrosion of C-Fe^0 was accelerated at lower pH values, and the rate of reaction was also accelerated (Li et al. 2012). The products of Fe^{2+} promoted the reductive conversion of Cr(VI) into Cr(III); thereby, the sequestration of Cr(VI) on C-Fe^0 might involve a combined reduction and co-precipitation processes. Figure 1B exhibited the efficiency of Cr(VI) sequestration as a function of C-Fe^0 dosage in the

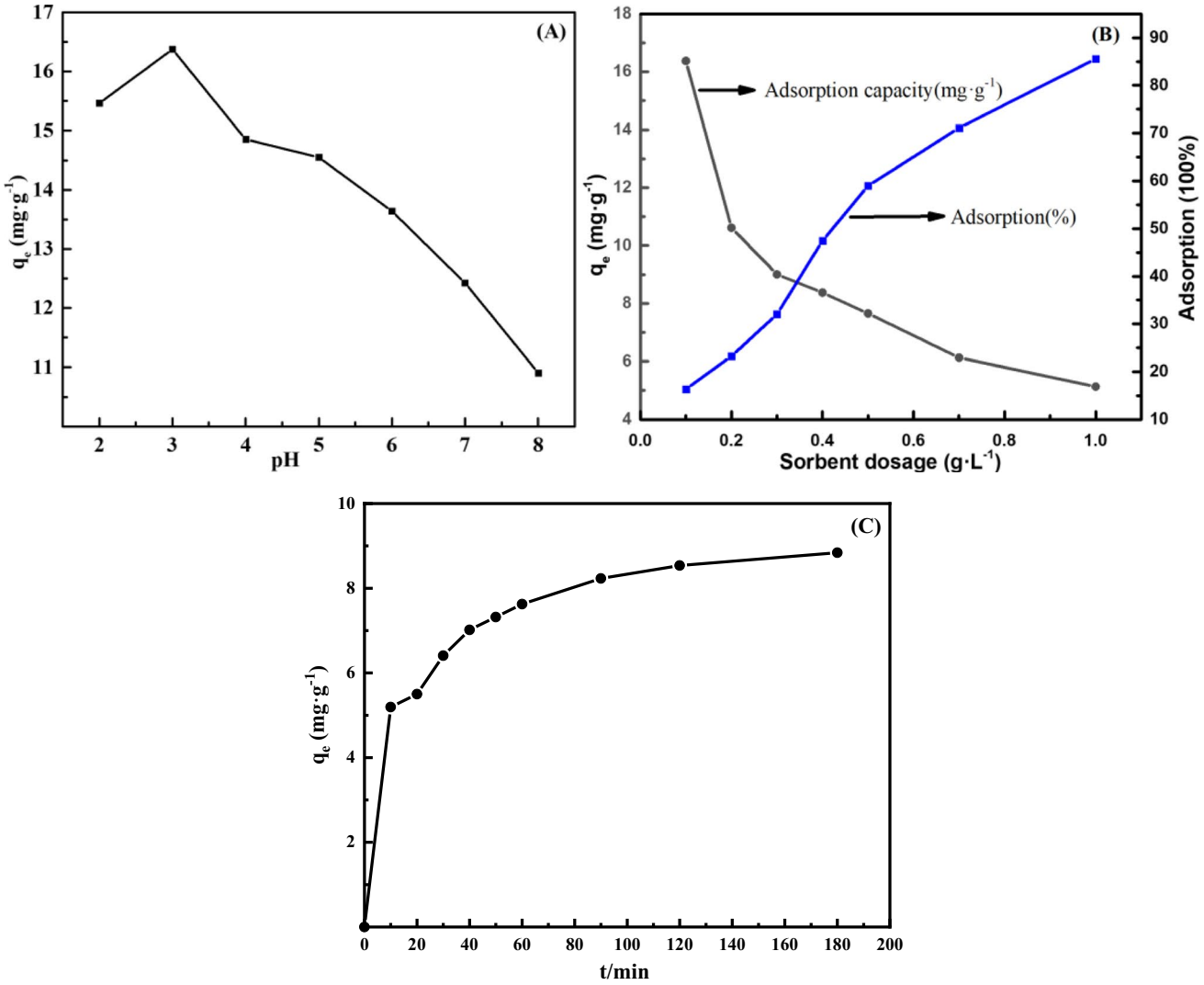

Fig. 1 The effect of pH (**A**), sorbent dosage (**B**), and reaction time (**C**), on the sequestration of Cr(VI) on C-Fe^0 material

range from 0.1 to 1.0 g/L, which exhibited that the increment in C-Fe^0 dosage was beneficial to the improvement in Cr(VI) sequestration efficiency. This result was mainly due to the factor that more C-Fe^0 dosage could supply more surface reactive sites for Cr(VI) sequestration (Li et al. 2021a; Soliemanzadeh and Fekri 2017). Besides, more C-Fe^0 addition would lead to the reduction of C-Fe^0 utilization and the inconvenience of separation. So it is necessary to choose a suitable C-Fe^0 dosage in the real application of Cr(VI) sequestration. The effect of contact time in Cr(VI) sequestration was also conducted in the adsorption experiment, and the results are displayed in Fig. 1C. The tend of Cr(VI) sequestration on C-Fe^0 surface increased sharply from 5 to 60 min, then slowed down from 60 to 120 min, and finally reached adsorption equilibrium. There was a large number of adsorption sites on C-Fe^0, and the high Cr(VI) concentration in solution makes it very easy to be removed on C-Fe^0 at the initial adsorption stage. With the adsorption progressing, the adsorption sites on C-Fe^0 surface and the Cr(VI) concentration decreased, and the adsorption slowed down until it reached equilibrium (Wang et al. 2022).

Figures 2 and 3 displayed the adsorption kinetics of Cr(VI) sequestration on C-Fe^0 as a function of pH, Cr(VI) concentration, and adsorbent dosage, and the related fitting of pseudo-first-order kinetic model, pseudo-second-order kinetics model, intraparticle diffusion model. It was generally reported that the adsorption kinetics of metal(loid)s can be fitted accurately by the pseudo-first-order kinetic model, pseudo-second-order kinetics model, intraparticle diffusion model (Kong et al. 2016; Shi et al. 2011a, b).

The pseudo-first-order kinetic model could be depicted as Eq. (1):

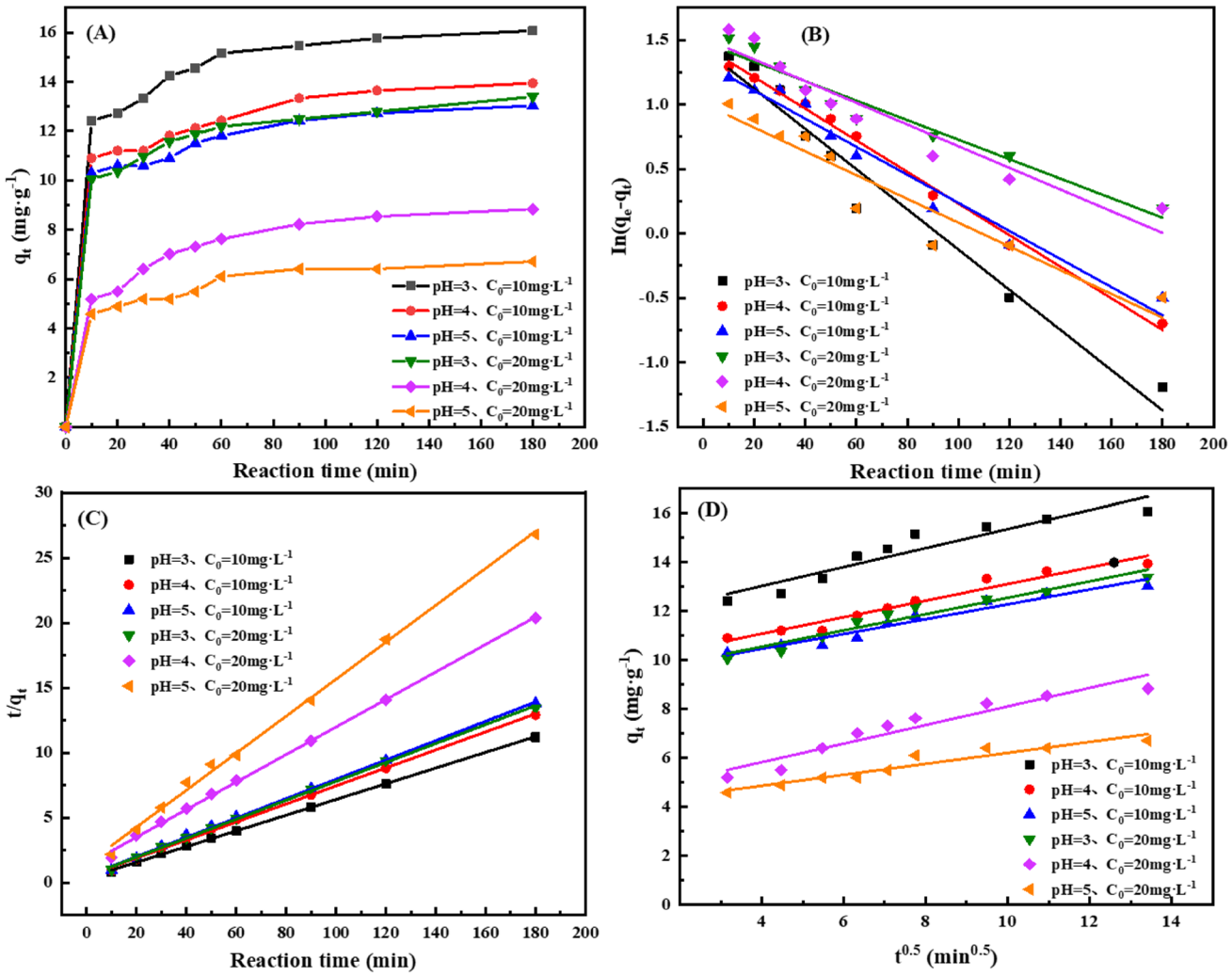

Fig. 2 The sequestration of Cr(VI) on C-Fe^0 as a function of pH and Cr(VI) concentration (**A**), and the related kinetic fitting of (**B**) pseudo-first-order kinetic model, (**C**) pseudo-second-order kinetics model, (**D**) intraparticle diffusion model

$$\log\left(q_e - q_t\right) = \log q_e - \frac{k_1 t}{2.303} \tag{1}$$

The pseudo-second-order kinetics model could be depicted as Eq. (2):

$$\frac{t}{q_t} = \frac{1}{k_2 q_e^2} + \frac{1}{q_e} t \tag{2}$$

The intraparticle diffusion model could be depicted as Eq. (3):

$$q_t = k_p t^{1/2} + I \tag{3}$$

where q_e (mg/g) and q_t (min) are the adsorption capacities at equilibrium and at time t, respectively, k_1 (min^{-1}) and k_2 (g/(mg min)) are the pseudo-first-order rate constant and pseudo-second-order rate constant, respectively, k_p (mg/(min$^{1/2}$ g)) is the intraparticle diffusion rate constant, and I is the intercept (Kong et al. 2016; Shi et al. 2011a, b). And the kinetic fitting parameters were all presented in Tables 1, 2, 3 and 4, respectively. Comparing the correlation coefficient value (R^2) for different modes, we can see that the pseudo-second-order model fitted the adsorption Cr(VI) on C-Fe^0 the best. So, the pseudo-second-order was dominant, and the potential rate-determining step in Cr(VI) adsorption on C-Fe^0 was chemical interaction which involved sharing and exchanging of electrons between the binding site and Cr(VI) ions (Gerente et al. 2007; Luo et al. 2015; Su et al. 2020).

The isotherm data is very important for depicting the adsorption state at equilibrium, which can provide the basic information about thermodynamic performance (Niu et al. 2013; Zhao et al. 2018). The isotherm adsorption curves of Cr(VI) sequestration on C-Fe^0 materials were shown in Fig. 4. We can clearly see that the adsorption increased

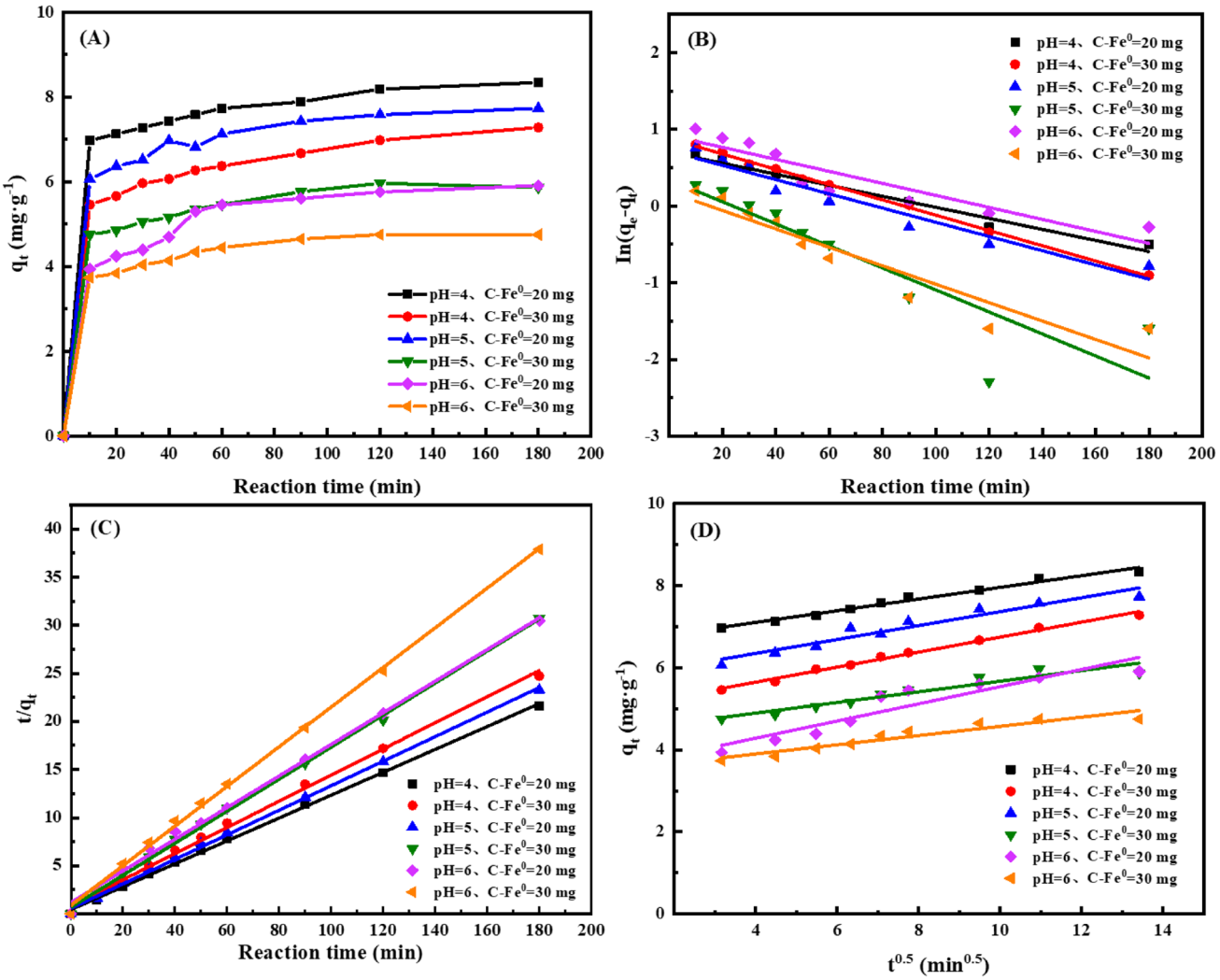

Fig. 3 The sequestration of Cr(VI) on C-Fe^0 as a function of pH and sorbent dosage (**A**), and the related kinetic fitting of (**B**) pseudo-first-order kinetic model, (**C**) pseudo-second-order kinetics model, (**D**) intraparticle diffusion model

Table 1 Fitting parameters of pseudo-first-order kinetic model for Cr(VI) adsorption

Model	Conditions		Parameters		
			K_1	q_e	R^2
Pseudo-first-order kinetic model	pH = 3 C-Fe^0 = 10 mg	C_0 = 5 mg L^{-1}	7.780 ± 0.001 × 10^{-3}	1.07 ± 0.01	0.9384 ± 0.0001
		C_0 = 10 mg L^{-1}	1.559 ± 0.001 × 10^{-2}	4.19 ± 0.01	0.9653 ± 0.0001
		C_0 = 20 mg L^{-1}	1.001 ± 0.001 × 10^{-2}	4.59 ± 0.01	0.7176 ± 0.0001
	pH = 4 C-Fe^0 = 10 mg	C_0 = 10 mg L^{-1}	1.063 ± 0.001 × 10^{-2}	4.11 ± 0.01	0.9815 ± 0.0001
		C_0 = 20 mg L^{-1}	8.418 ± 0.001 × 10^{-3}	4.56 ± 0.01	0.9188 ± 0.0001
	pH = 5 C-Fe^0 = 10 mg	C_0 = 10 mg L^{-1}	1.436 ± 0.001 × 10^{-2}	4.32 ± 0.01	0.9416 ± 0.0001
		C_0 = 20 mg L^{-1}	1.225 ± 0.001 × 10^{-2}	4.29 ± 0.01	0.9948 ± 0.0001
	pH = 4 C_0 = 10 mg L^{-1}	C-Fe^0 = 20 mg	1.088 ± 0.001 × 10^{-2}	3.76 ± 0.01	0.9707 ± 0.0001
		C-Fe^0 = 30 mg	7.560 ± 0.001 × 10^{-3}	4.41 ± 0.01	0.9518 ± 0.0001
	pH = 5 C_0 = 10 mg L^{-1}	C-Fe^0 = 20 mg	9.957 ± 0.001 × 10^{-3}	3.97 ± 0.01	0.9337 ± 0.0001
		C-Fe^0 = 30 mg	9.210 ± 0.001 × 10^{-3}	2.73 ± 0.01	09,133 ± 0.0001
	pH = 6 C_0 = 10 mg L^{-1}	C-Fe^0 = 20 mg	1.755 ± 0.001 × 10^{-2}	4.42 ± 0.01	0.9683 ± 0.0001
		C-Fe^0 = 30 mg	9.970 ± 0.001 × 10^{-3}	2.41 ± 0.01	0.9978 ± 0.0001

Table 2 Fitting parameters of pseudo-second-order model for Cr(VI) adsorption

Model	Conditions		Parameters		
			K_2	q_e	R^2
Pseudo-second-order kinetics model	pH = 3 C-Fe^0 = 10 mg	C_0 = 5 mg L^{-1}	1.421 ± 0.001 × 10^{-2}	7.325 ± 0.001	0.9979 ± 0.0001
		C_0 = 10 mg L^{-1}	1.010 ± 0.001 × 10^{-2}	15.88 ± 0.01	0.9991 ± 0.0001
		C_0 = 20 mg L^{-1}	4.533 ± 0.001 × 10^{-1}	12.43 ± 0.01	0.9998 ± 0.0001
	pH = 4 C-Fe^0 = 10 mg	C_0 = 10 mg L^{-1}	9.541 ± 0.001 × 10^{-3}	11.81 ± 0.01	0.9998 ± 0.0001
		C_0 = 20 mg L^{-1}	1.083 ± 0.001 × 10^{-2}	11.24 ± 0.01	0.9991 ± 0.0001
	pH = 5 C-Fe^0 = 10 mg	C_0 = 10 mg L^{-1}	1.052 ± 0.001 × 10^{-2}	8.432 ± 0.001	0.9987 ± 0.0001
		C_0 = 20 mg L^{-1}	4.533 ± 0.001 × 10^{-1}	5.347 ± 0.001	0.9998 ± 0.0001
	pH = 4 C_0 = 10 mg L^{-1}	C − Fe^0 = 20 mg	2.436 ± 0.001 × 10^{-2}	8.739 ± 0.001	0.9969 ± 0.0001
		C − Fe^0 = 30 mg	1.010 ± 0.001 × 10^{-2}	7.437 ± 0.001	0.9991 ± 0.0001
	pH = 5 C_0 = 10 mg L^{-1}	C − Fe^0 = 20 mg	1.886 ± 0.001 × 10^{-2}	6.862 ± 0.001	0.9997 ± 0.0001
		C − Fe^0 = 30 mg	3.713 ± 0.001 × 10^{-2}	5.054 ± 0.001	0.9998 ± 0.0001
	pH = 6 C_0 = 10 mg L^{-1}	C − Fe^0 = 20 mg	3.089 ± 0.001 × 10^{-2}	4.964 ± 0.001	0.9988 ± 0.0001
		C − Fe^0 = 30 mg	5.245 ± 0.001 × 10^{-2}	4.232 ± 0.001	0.9992 ± 0.0001

Table 3 Fitting parameters of intraparticle diffusion model for Cr(VI) adsorption

Model	Conditions		Parameters		
			k_i	I	R^2
Intraparticle diffusion model	pH = 3 C-Fe^0 = 10 mg	C_0 = 5 mg L^{-1}	0.3859 ± 0.0001	11.48 ± 0.01	0.8933 ± 0.0001
		C_0 = 10 mg L^{-1}	0.2859 ± 0.0001	8.469 ± 0.001	0.9157 ± 0.0001
		C_0 = 20 mg L^{-1}	0.4127 ± 0.0001	7.426 ± 0.001	0.9465 ± 0.0001
	pH = 4 C-Fe^0 = 10 mg	C_0 = 10 mg L^{-1}	0.3388 ± 0.0001	9.724 ± 0.001	0.9543 ± 0.0001
		C_0 = 20 mg L^{-1}	0.3032 ± 0.0001	9.251 ± 0.001	0.9477 ± 0.0001
	pH = 5 C-Fe^0 = 10 mg	C_0 = 10 mg L^{-1}	0.3336 ± 0.0001	9.218 ± 0.001	0.9422 ± 0.0001
		C_0 = 20 mg L^{-1}	0.3796 ± 0.0001	4.313 ± 0.001	0.9155 ± 0.0001
	pH = 4 C_0 = 10 mg L^{-1}	C-Fe^0 = 20 mg	0.2242 ± 0.0001	3.969 ± 0.001	0.9173 ± 0.0001
		C-Fe^0 = 30 mg	0.3174 ± 0.0001	10.46 ± 0.001	0.9590 ± 0.0001
	pH = 5 C_0 = 10 mg L^{-1}	C-Fe^0 = 20 mg	0.1828 ± 0.0001	4.918 ± 0.001	0.9911 ± 0.0001
		C-Fe^0 = 30 mg	0.1134 ± 0.0001	3.566 ± 0.001	0.7261 ± 0.0001
	pH = 6 C_0 = 10 mg L^{-1}	C-Fe^0 = 20 mg	0.1295 ± 0.0001	4.377 ± 0.001	0.9091 ± 0.0001
		C-Fe^0 = 30 mg	0.4216 ± 0.0001	3.801 ± 0.001	0.9169 ± 0.0001

with the increase of initial Cr(VI) concentration, suggesting that the adsorption of Cr(VI) on C-Fe^0 favored high concentration because of the larger driving force that arose from high concentration gradient (Zhao et al. 2018). Herein, the Langmuir, Dubinin-Radushkevich (D-R), and Freundlich isotherm models were used to described the isotherm adsorption data, in order to reveal the isotherm adsorption mechanism (Niu et al. 2013, 2014; Zhao et al. 2018).

The linear equation of Langmuir model could be depicted by Eq. (4):

$$\frac{C_e}{q_e} = \frac{C_e}{q_m} + \frac{1}{q_m K_L} \tag{4}$$

The linear equation of Freundlich model could be depicted by Eq. (5):

$$lnq_e = lnK_F + \frac{lnC_e}{n} \tag{5}$$

The linear equation of D-R model could be depicted by Eq. (6):

$$lnq_e = lnq_m - \beta\varepsilon^2 \tag{6}$$

where C_e (mg L^{-1}) and q_e (mg g^{-1}) are the equilibrium Cr(VI) concentration and adsorption capacity, respectively, q_m (mg g^{-1}) is the maximum adsorption amount, K_L (L mg^{-1}) is the Langmuir constant, K_F (mg·g^{-1}) is the Freundlich constant, and n is adsorption intensity index related to adsorption intensity. Besides, ε (kJ^2 mol^{-2}) is a Polanyi potential that could be obtained by $\varepsilon = RT\ln(1 + 1/C_e)$, β (mol^2 J^{-2}) is an activity coefficient that was related to a mean

Table 4 Fitting parameters of XPS analysis of C-Fe^0 before and after reaction

Elements	Bond species	C-Fe^0	C-Fe^0/Cr
O	O–Fe	529.8	529.3
	O–Cr		528.8
	O–H	532.6	532.5
	O–C	531.3	531.1
	O=C	533.8	533.5
Fe	Fe^0	706.8	
	Fe(III)	710.8, 719.1	710.9, 719.8
	FeOOH	724.8	724.9
Cr	Cr_2O_3		576.1
	$Cr(OH)_3$		586.2
	Cr(III)-Fe(III)		577.9
	Cr(VI)		587.9

free energy (E, kJ mol^{-1}). The E value could be derived by this relationship, $E = \frac{1}{\sqrt{2\beta}}$. We can use the E value to determine whether the adsorption of Cr(VI) is physical or chemical. When the value of E is below 8 kJ mol^{-1}, it indicates a physical adsorption. When the E value was in the range of 8–16 kJ mol^{-1}, it suggests a chemical adsorption (Zhao et al. 2018). According to the fitting parameters, we can see that the correlation coefficient of Langmuir ($R_L{}^2$, 0.994) was higher than Freundlich ($R_F{}^2$, 0.985) and the D-R model ($R_{D\text{-}R}{}^2$, 0.962), indicating the adsorption of Cr(VI) on C-Fe^0 can be the best depicted by Langmuir model with a monolayer adsorption. In addition, the E value was determined to be in the range of 8–16 kJ mol^{-1}, which indicated the adsorption of C-Fe^0 for Cr(VI) was chemical interaction in nature.

Characterization results and mechanism insights

Herein, various characterization methods were used to reveal the structural changes of the materials before and after reaction. Figure 5 presented the SEM of celite, and C-Fe^0, as well as TEM and EDS mapping of C-Fe^0 before reaction. It could be seen from SEM that there existed a little of pores on celite particles with some discal structure, which make it a good possibility for Fe^0 to be decorated on celite surfaces. According to the SEM and TEM of C-Fe^0, we could observe that the shaped Fe^0 particles were dispersed on celite surfaces. Elemental analysis from EDS mapping showed the presence of Fe, Si, O, and to a smaller extent of Ca, which further indicated the successful combination of Fe^0 and celite. Figure 6 presented the FTIR spectra, and XRD patterns of C-Fe^0 before and after reaction with Cr(VI). In the FTIR spectra, the band at ~ 3400 cm^{-1} might be caused by the stretching vibration of Si–OH group, the band at ~ 1020 cm^{-1} might be attributed to the bending vibration of Si–OH, the band at ~ 540 cm^{-1} might be attributed to the bending vibration of

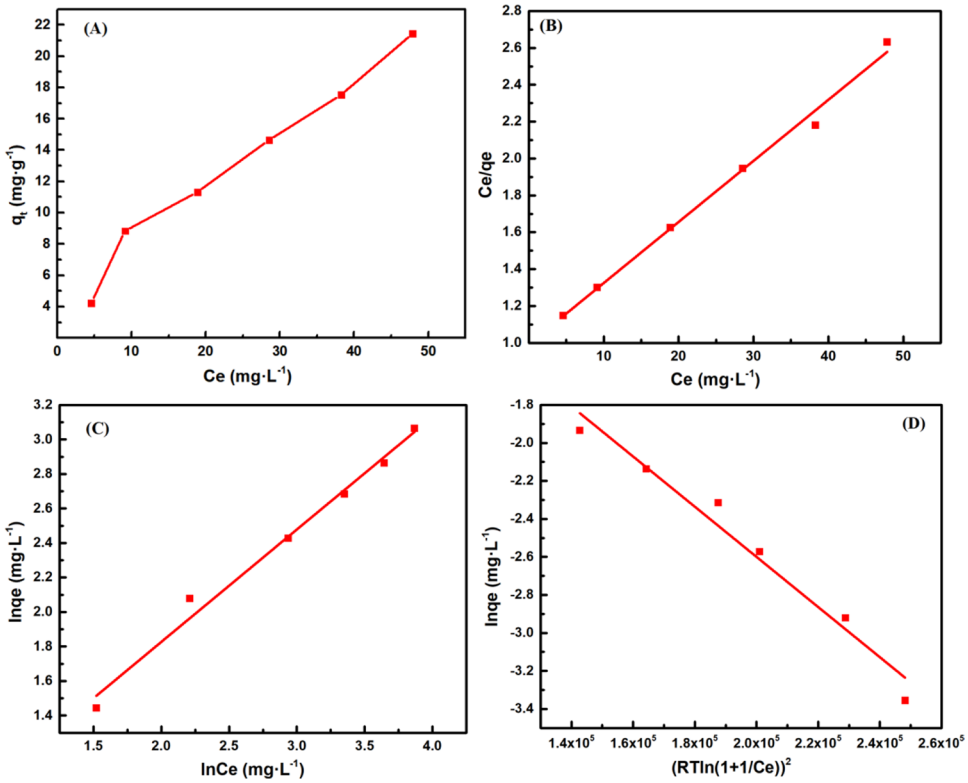

Fig. 4 The adsorption isotherm of Cr(VI) sequestration on C-Fe^0 material (**A**), Langmuir model (**B**), Freundlich model (**C**), and D–R model (**D**) fitting results

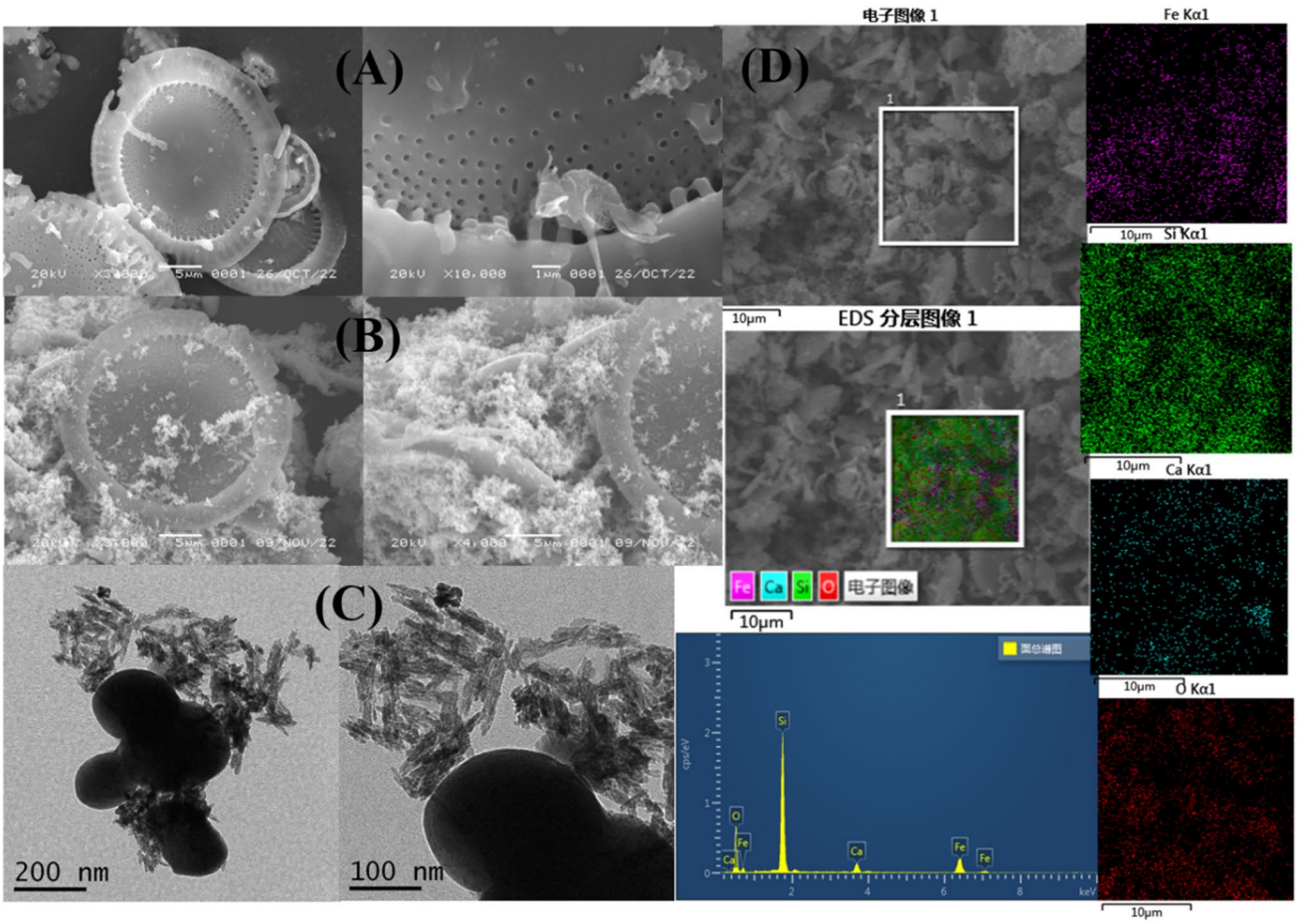

Fig. 5 SEM images of (**A**) celite, and (**B**) C-Fe^0 samples, and TEM images of (**C**) C-Fe^0, as well as SEM–EDS mapping of (**D**) C-Fe^0 before reaction

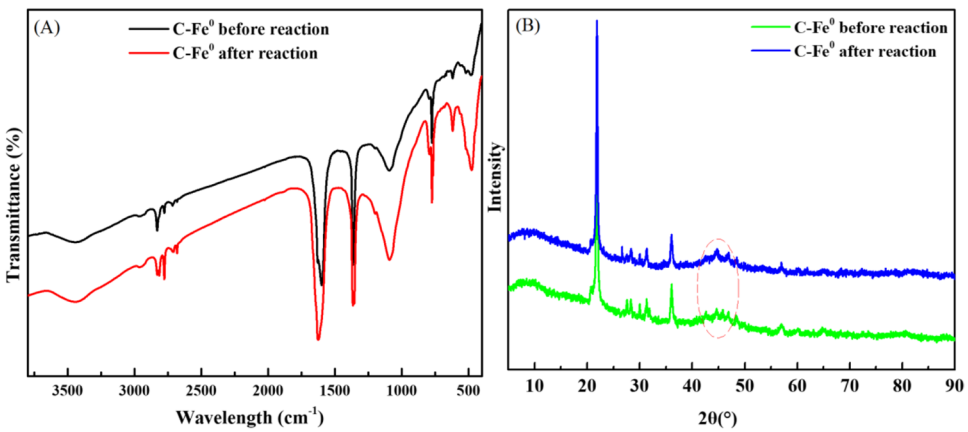

Fig. 6 FTIR spectra (**A**), and XRD patterns (**B**) of C-Fe.^{0} samples before and after reaction with Cr(VI)

Fe–O. The intensity change of these bands before and after reaction suggess the chemical interaction between Cr(VI) and C-Fe^0. Meanwhile, the XRD patterns indicated that C-Fe^0 before and after reaction was poorly crystallized. It revealed that both samples consist of SiO_2 with some other oxides. Besides, the reflection at 2θ ~ 44.5° was indicative of iron (Jing et al. 2015; Xu et al. 2014). Figure 7 showed the nitrogen adsorption–desorption isotherms and pore distributions of C-Fe^0. The BET surface area of C-Fe^0 was 9.24 m^2/g, and the corresponding pore size (adsorption average pore width) is 11.8 nm, respectively. Figure 8 showed the SEM, TEM, and EDS mapping of C-Fe^0 after reaction with

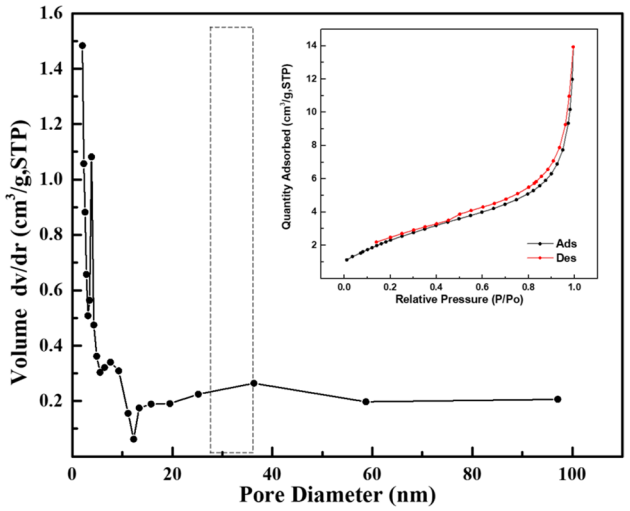

Fig. 7 Nitrogen adsorption–desorption isotherms and pore distributions of C-Fe.^{0}

Cr(VI). Compared with the EDS mapping of C-Fe^0 before reaction, elemental analysis showed additional Cr in EDS mapping of C-Fe^0 after reaction, suggesting the surface reaction of C-Fe^0 and Cr(VI). The surface became scabrous after reacting with Cr(VI) and the chain-like aggregates of Fe^0 became more clear, which might be resulted from the gradual cover of iron oxide layers like FeOOH and Fe_2O_3 on C-Fe^0 surface (Chen et al. 2011).

It has been widely believed that Cr(VI) sequestration by iron and its composites involved a combined processes of physical adsorption and chemical reduction (Wang et al. 2020). So, in the present work, XPS analysis was conducted for characterization of C-Fe^0 before and after reaction of Cr(VI). Figure 9 showed the surveyed XPS spectra of C-Fe^0 before and after reaction with Cr(VI), as well as the corresponding high XPS spectra of Cr2p, O1s, and Fe2p, before and after reaction with Cr(VI). Binding energies of O1s at ~ 528 eV, ~ 529 eV, ~ 531 eV, ~ 53 2 eV, and 533 eV were assigned to O–Cr, O–Fe, O–C, O–H, and O = C, respectively (Li et al. 2022; Wang et al.

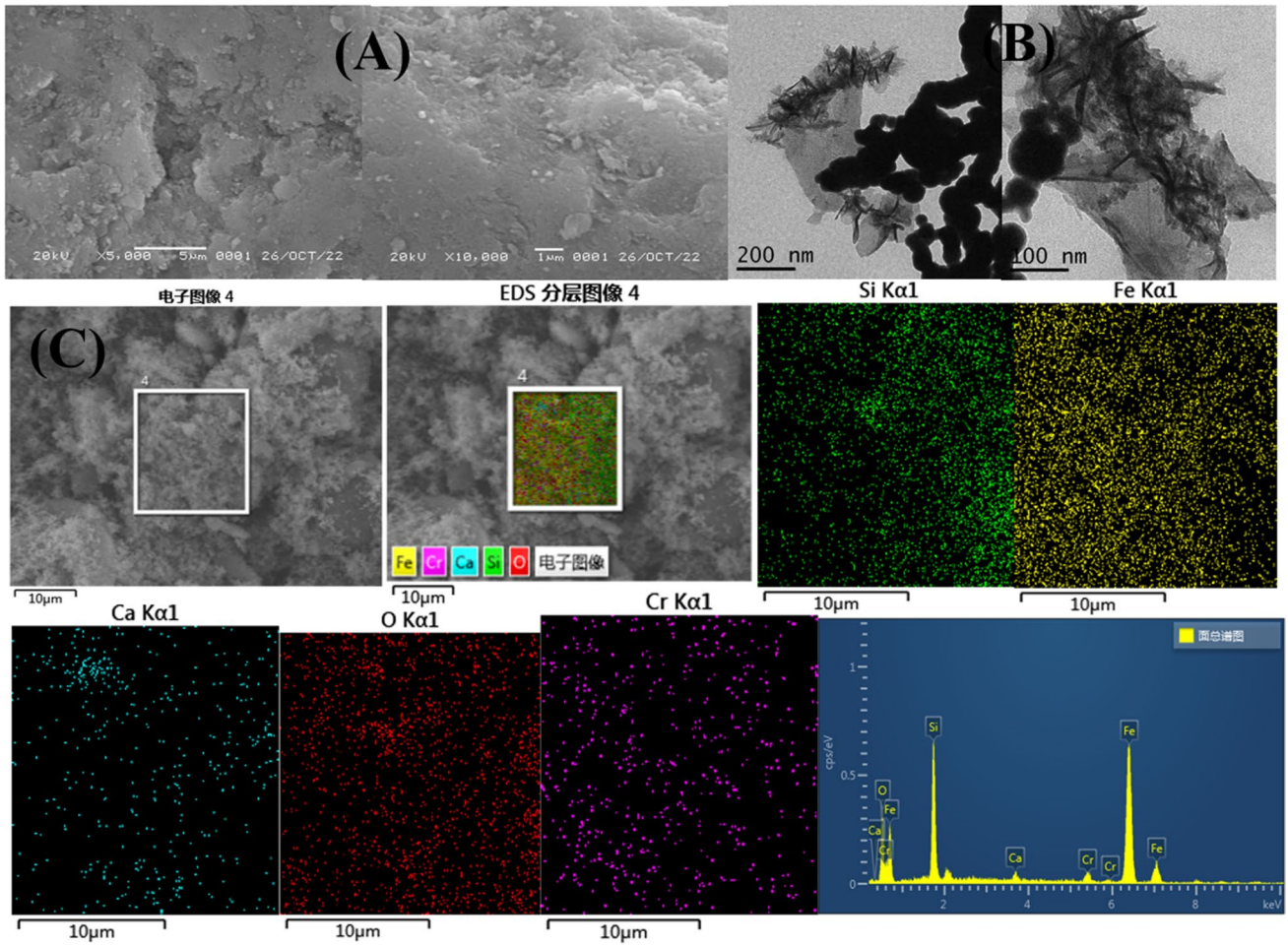

Fig. 8 SEM images (**A**), and TEM images (**B**), as well as SEM–EDS mapping (**C**) of C-Fe.^{0} after reaction with Cr(VI)

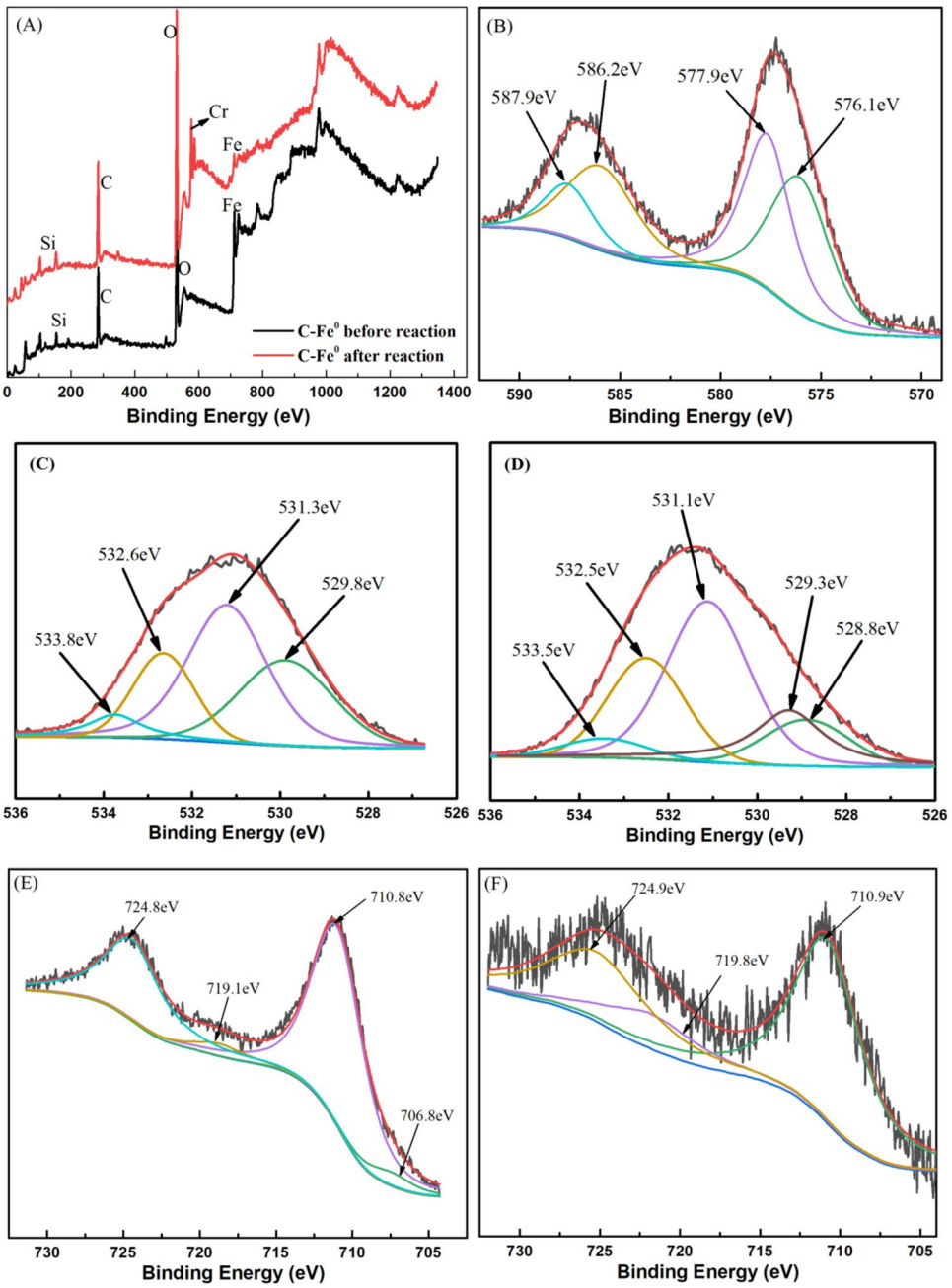

Fig. 9 The surveyed XPS spectra of C-Fe.^{0} before and after reaction with Cr(VI) (**A**), as well as the high XPS spectra of Cr1s (**B**), O1s before (**C**), and after (**D**), reaction with Cr(VI), Fe2p before (**E**), and after (**F**), reaction with Cr(VI)

2020; Wu et al. 2020), suggesting that surface complexation had an important effect on Cr(VI) sequestration. The Fe2p spectrum has three peaks, namely, Fe^0 at ~ 706 eV, Fe(III) at ~ 710 eV, and FeOOH at ~ 724 eV; meanwhile, the Cr2p spectrum has four peaks, i.e., Cr_2O_3 at ~ 576 eV, Cr(III)-Fe(III) at ~ 577 eV, $Cr(OH)_3$ at ~ 586 eV, and Cr(VI) at ~ 587 eV (Lyu et al. 2017, 2018; Wang et al. 2020; Wu et al. 2020), which proved the reduction reaction between Cr(VI) and C-Fe^0. It was reported by Wang et al. (2020) that Cr(VI) sequestration on Fe^0-based composites followed a common process. Namely, when Fe^0-based composites contacted with Cr(VI), electrons could directly transfer from Fe^0 to Cr(VI); thus, reduction of Cr(VI) by Fe^0 is favorable (Eq. (7)). Then, reduction between Cr(VI) and Fe(II) could spontaneously happen, which reduces Cr(VI) indirectly into Cr(III) (Eq. (8)). Meanwhile, these reactive Fe(II) species could be constantly generated through electron transfer among different Fe species (Eqs. (9) and (10)). Finally, Cr(VI)–Fe(III) and Cr(III)–Fe(III) precipitation, as well as iron oxides could be formed on solid surface because of pH variations during the reaction (Eqs. (11)–(13)) (Wang et al. 2020).

$$2HCrO_4^- + 14H^+ + 3Fe^0 \rightarrow 3Fe^{2+} + 8H_2O \quad (7)$$

$$HCrO_4^- + 7H^+ + 3Fe^{2+} \rightarrow Cr^{3+} + 4H_2O + 3Fe^{3+} \quad (8)$$

$$Fe^0 - 2e^- \rightarrow Fe^{2+} \quad (9)$$

$$2Fe^0 - Fe^0 \rightarrow 3Fe^{2+} \quad (10)$$

$$2Fe^{3+} + 6OH^- \rightarrow 2Fe(OH)_3(s) \rightarrow Fe_2O_3(s)3H_2O \quad (11)$$

$$Fe^{2+} + Cr_2O_4^{2-} \rightarrow FeCr_2O_4(s) \quad (12)$$

$$2Cr^{3+} + 6OH^- \rightarrow 2Cr(OH)_3(s) \rightarrow Cr_2O_3(s)3H_2O \quad (13)$$

Combining previous reports (Lv et al. 2017) and the observed results herein, we could conclude that Cr(VI) sequestration on C-Fe^0 was mainly composed of both adsorption and reduction. Firstly, abundant Cr(VI) in solution could be quickly adsorbed onto C-Fe^0 surface and gradually diffused into interior of C-Fe^0, which confirmed with rapid decrease of Cr(VI) at the initial stage. When contacted with C-Fe^0, these adsorbed Cr(VI) were reduced into Cr(III). After that, some of these Cr species released back into solution. Besides, C-Fe^0 were oxidized to Fe^{2+} during reaction, which could continue to participate in Cr(VI) reduction. Finally, released Cr(III), Fe^{2+}, and Fe^{3+}, as well as remaining Cr(VI) co-precipitated as Cr(III)-Fe(III) (oxy)hydroxides to further remove Cr(VI) from aqueous solution (Lv et al. 2017). The findings indicated that C-Fe^0 was a good material for Cr(VI) sequestration.

Conclusions

In the present paper, novel composites namely celite decorated iron nanoparticles (C-Fe^0) were prepared by an in situ reduction method, and the sequestration performance of Cr(VI) by C-Fe^0 from aqueous solution was evaluated. The influence of ambient conditions, including solution pH, adsorbent dosage, and initial Cr(VI) concentration on Cr(VI) sequestration performance, was studied. The results indicated that increasing pH exhibited the most significantly negative effect on Cr(VI) sequestration. Kinetics study indicated that pseudo-second-order adsorption model was more suitable to describe the Cr(VI) sequestration, and the Langmuir adsorption model fitted the best with the isotherm data of Cr(VI) adsorption on C-Fe^0. Finally, the possible Cr(VI) sequestration path by C-Fe^0 was analyzed. In general, the C-Fe^0 exhibits many advantages as low cost and environmental benignity, providing an admirable alternative over the common methods in Cr(VI) remediation.

Acknowledgements We sincerely thank the young and middle-aged academic cadres from Shaoxing University. This work was also supported by the Opening Project of Zhejiang Engineering Research Center of Fat-soluble Vitamin.

Author contribution Data curation, visualization, methodology, investigation, formal analysis were performed by XC, JC, and HL. The first draft of the manuscript was written by XC and GS. Writing—review and editing, formal analysis were performed by GS.

Data availability All data and models that support the findings of this study are available from the corresponding author upon reasonable request.

Declarations

Ethics approval Ethical approval is not applicable, because this article does not contain any studies with human or animal subjects.

Consent to participate Not applicable.

Consent for publication Not applicable.

Competing interests The authors declare no competing interests.

References

Abbasi N, Khan SA, Liu Z (2023) Natural deep eutectic solvent (fructose-glycine) functionalized-celite/ polyethylene glycol hydrogel nanocomposite for phosphate adsorption: Statistical analysis. J Environ Manage 330:117206

Awual MdR, Khraisheh M, Alharthi NH et al (2018) Efficient detection and adsorption of cadmium(II) ions using innovative nanocomposite materials. Chem Eng J 343:118–127

Boglaienko D, Emerson HP, Katsenovich YP et al (2019) Comparative analysis of ZVI materials for reductive separation of ^{99}Tc(VII) from aqueous waste streams. J Hazard Mater 380:120836

Bone SE, Dynes JJ, Cliff J et al (2017) Uranium (IV) adsorption by natural organic matter in anoxic sediments. P Nati Acad Sci USA 114:711–716

Chang SF, Chang SW, Yen YH et al (2007) Optimum immobilization of *Candida rugosa* lipase on celite by RSM. Appl Clay Sci 37:67–73

Chen Z, Jin X, Chen Z et al (2011) Removal of methyl orange from aqueous solution using bentonite-supported nanoscale zero-valent iron. J Colloid Interface Sci 363:601–607

Chen A, Shang C, Shao J et al (2017) The application of iron-based technologies in uranium remediation: a review. Sci Total Environ 575:1291–1306

Chen J, Wu H, Xu L et al (2021) New insights into colloidal GO, Cr(VI) and Fe(II) interaction by a combined batch, spectroscopic and DFT calculation investigation. J Mol Liq 337:116365

Chen J, Wu H, Sheng G et al (2022) Graphene oxide-mediated the reduction of U(VI), Re(VII), Se(VI) and Se(IV) by Fe(II) in aqueous solutions investigated via combined batch, DFT calculation and spectroscopic approaches. Chem Eng J 433:133844

Chen J, Cheng X, Sheng G (2023) Graphene oxide enhanced the reductive sequestration of UO_2^{2+}, ReO_4^-, SeO_4^{2-} and SeO_3^{2-} by zero-valent iron: batch, column and mechanism investigations. J Radioanal Nucl Chem https://doi.org/10.1007/s10967-022-08725-z.

Dong L, Liao Q, Linghu W et al (2018) Application of EXAFS with a bent crystal analyzer to study the pH dependent microstructure of Eu(III) onto birnessite. J Environ Chem Eng 6:842–848
Dong L, Li S, Jin Y et al (2021) Enhanced adsorption of Eu(III) from wastewater using Solidago canadensis-derived biochar functionalized by Ca/Al-LDH and hydroxyapatite. Appl Surf Sci 567:150794
Fan P, Sun Y, Lei H et al (2023) Mechanochemically ball-milled zerovalent iron and ferrous composite for effective removal of various metal(loid)s from water. Chem Eng J 452:139380
Flynn ED, Catalano JG (2017) Competitive and cooperative effects during nickel adsorption to iron oxides in the presence of oxalate. Environ Sci Technol 51:9792–9799
Ge T, Jiang Z, Shen L et al (2021) Synthesis and application of $Fe_3O_4/FeWO_4$ composite as an efficient and magnetically recoverable visible light-driven photocatalyst for the reduction of Cr(VI). Sep Purif Technol 263:118401
Gerente C, Lee VKC, Cloirec PL et al (2007) Application of chitosan for the removal of metals from wastewaters by adsorption—mechanisms and models review, Critical Reviews in Environ. Sci Technol 37:41–127
Gu Z, Deng B, Yang J (2007) Synthesis and evaluation of iron-containing ordered mesoporous carbon (FeOMC) for arsenic adsorption. Microporous Mesoporous Mater 102:265–273
Gu H, Liu X, Wang S et al (2022) COF-based composites: extraordinary removal performance for heavy metals and radionuclides from aqueous solutions. Rev Environ Contam Toxicol 260:23
Hao M, Liu Y, Wu W et al (2023) Advanced porous adsorbents for radionuclides elimination. EnergyChem. https://doi.org/10.1016/j.enchem.2023.100101
Hong S, Lyonga F, Kang J et al (2020) Synthesis of Fe-impregnated biochar from food waste for selenium (VI) removal from aqueous solution through adsorption: Process optimization and assessment. Chemosphere 252:126475
Hu X, Wang Y, Ouyang J et al (2020) Synthesis of graphene oxide nanoribbons/chitosan composite membranes for the removal of uranium from aqueous solutions. Front Chem Sci Eng 14:1029–1038
Jabli M, Almalki SG, Agougui H (2020) An insight into methylene blue adsorption characteristics onto functionalized alginate bio-polymer gel beads with λ-carrageenan-calcium phosphate, carboxymethyl cellulose, and celite 545. Int J Biol Macromol 156:1091–1103
Jing C, Li Y, Cui R et al (2015) Illite-supported nanoscale zero-valent iron for removal of ^{238}U from aqueous solution: characterization, reactivity and mechanism. J Radioanal Nucl Chem 304:859–865
Kang L, Yang H, Wang L et al (2020) Facile integration of FeS and titanate nanotubes for efficient removal of total Cr from aqueous solution: synergy in simultaneous reduction of Cr(VI) and adsorption of Cr(III). J Hazard Mater 398:122834
Kong X, Han Z, Zhang W et al (2016) Synthesis of zeolite-supported microscale zero-valent iron for the removal of Cr^{6+} and Cd^{2+} from aqueous solution. J Environ Manage 169:84–90
Kou J, Wei X, Wu H et al (2022) Efficient adsorptive and reductive removal of U(VI) and Se(IV) using porous hexagonal boron nitride supported nanoscale iron sulfide: performance and mechanism. J Mol Liq 359:119355
Li S, Wu P, Li H et al (2010) Synthesis and characterization of organo-montmorillonite supported iron nanoparticles. Appl Clay Sci 50:330–336
Li Y, Li J, Zhang Y (2012) Mechanism insights into enhanced Cr(VI) removal using nanoscale zerovalent iron supported on the pillared bentonite by macroscopic and spectroscopic studies. J Hazard Mater 227:211–218
Li X, Ai L, Jiang J (2016) Nanoscale zerovalent iron decorated on graphene nanosheets for Cr(VI) removal from aqueous solution: surface corrosion retard induced the enhanced performance. Chem Eng J 288:789–797
Li W, Dong X, Zhu L et al (2020) Highly selective separation of Re(VII) from Mo(VI) by using biomaterial-based ionic gel adsorbents: extractive adsorption enrichment of Re and surface blocking of Mo. Chem Eng J 387:124078
Li L, Wu H, Chen J et al (2021a) Anchoring nanoscale iron sulfide onto graphene oxide for the highly efficient immobilization of uranium(VI) from aqueous solutions. J Mol Liq 332:115910
Li M, Ji Z, Sheng G et al (2021b) Scavenging mechanism of rare earth metal ions in water by graphene oxide. J Mol Liq 322:114940
Li L, Chen J, Sheng G et al (2022) Enhanced performance for total Cr removal using a novel h-BN supported nanoscale iron sulfide composite: stabilization effects and removal mechanism. Colloids Surf A 637:128239
Ling L, Liu W, Zhang S et al (2017) Magnesium oxide embedded nitrogen self-doped biochar composites: fast and high-efficiency adsorption of heavy metals in an aqueous solution. Environ Sci Technol 51:10081–10089
Liu C, Lin Y, Chen C et al (2009) Characterization of *Burkholderia* lipase immobilized on celite carriers. J Taiwan Inst Chem E 40:359–436
Liu T, Wang Z, Yan X et al (2014) Removal of mercury (II) and chromium (VI) from wastewater using a new and effective composite: pumice-supported nanoscale zero-valent iron. Chem Eng J 245:34–40
Liu K, Zhao D, Hu Z et al (2023) The adsorption and reduction of anionic Cr(VI) in groundwater by novel iron carbide loaded on N-doped carbon nanotubes: effects of Fe-confinement. Chem Eng J 452:139357
Lu J, Fu F, Zhang L et al (2018) Insight into efficient co-removal of Se(IV) and Cr(VI) by magnetic mesoporous carbon microspheres: performance and mechanism. Chem Eng J 346:590–599
Luo J, Luo X, Crittenden J (2015) Removal of antimonite (Sb(III)) and antimonate (Sb(V)) from aqueous solution using carbon nanofibers that are decorated with zirconium oxide (ZrO_2). Environ Sci Technol 49:11115–11124
Lv X, Zhang Y, Fu W et al (2017) Zero-valent iron nanoparticles embedded into reduced graphene oxidealginate beads for efficient chromium (VI) removal. J Colloid Interface Sci 506:633–643
Lyu H, Tang J, Huang Y et al (2017) Removal of hexavalent chromium from aqueous solutions by a novel biochar supported nanoscale iron sulfide composite. Chem Eng J 322:516–524
Lyu H, Zhao H, Tang J et al (2018) Immobilization of hexavalent chromium in contaminated soils using biochar supported nanoscale iron sulfide composite. Chemosphere 194:360–369
Meunier SM, Rajabzadeh AR, Legge RL (2014) Kinetic modelling of the production of methyl oleate by Celite® supported lipase sol-gels. Biochem Eng J 85:63–70
Mukherjee K, Saha R, Ghosh A et al (2014) Surfactant-assisted bioremediation of hexavalent chromium by use of an aqueous extract of sugarcane Bagasse. Res Chem Intermed 40:1727–1734
Mukherjee K, Nandi R, Saha D et al (2015a) Surfactant-assisted bioremediation of hexavalent chromium from contaminated water. Desalin Water Treat 53(3):746–751
Mukherjee K, Nandi R, Saha D et al (2015b) Surfactant-assisted enhancement of bioremediation rate for hexavalent chromium by water extract of Sajina (Moringa oleifera) flower. Desalin Water Treat 54(2):525–532
Mukherjee K, Ghosh D, Saha B (2016) Reliable bioremediation of hexavalent chromium from wastewater using mango leaves as reductant in association with the neutral and anionic micellar aggregation as redox accelerators. Desalin Water Treat 57(36):16919–16926

Nandi R, Laskar S, Saha B (2017) Surfactant-promoted enhancement in bioremediation of hexavalent chromium to trivalent chromium by naturally occurring wall algae. Res Chem Intermed 43:1619–1634

Niu Y, Qu R, Sun C et al (2013) Adsorption of Pb(II) from aqueous solution by silica-gel supported hyperbranched poly–amidoamine dendrimers. J Hazard Mater 244–245:276–286

Niu Y, Qu R, Chen H et al (2014) Synthesis of silica gel supported salicylaldehyde modified PAMAM dendrimers for the effective removal of Hg(II) from aqueous solution. J Hazard Mater 278:267–278

Pan Y, Zhang C, Sheng G et al (2023) Highly efficient scavenging of uranium(VI) by molybdenum disulfide loaded ferrous sulfide composites: Kinetics, thermodynamics and mechanism aspects. J Taiwan Inst Chem E 142:104614

Saha B, Orvig C (2010) Biosorbents for hexavalent chromium elimination from industrial and municipal effluents. Coord Chem Rev 254(23–24):2959–2972

Saha R, Nandi R, Saha B (2011) Sources and toxicity of hexavalent chromium. J Coord Chem 64(10):1782–1806

Saha R, Saha I, Nandi R et al (2013a) Application of chattim tree (devil tree, alstonia scholaris) saw dust as a biosorbent for removal of hexavalent chromium from contaminated water. Can J Chem Eng 91(5):814–821

Saha R, Mukherjee K, Saha I (2013b) Removal of hexavalent chromium from water by adsorption on mosambi (Citrus limetta) peel. Res Chem Intermed 39:2245–2257

Saha R, Saha B (2014) Removal of hexavalent chromium from contaminated water by adsorption using mango leaves (Mangifera indica). Desalin Water Treat 52(10–12):1928–1936

Saslow SA, Um W, Pearce CI et al (2018) Cr(VI) effect on Tc-99 removal from Hanford low-activity waste simulant by ferrous hydroxide. Environ Sci Technol 52:11752–11759

Satar R, Husain Q (2009) Applications of Celite-adsorbed white radish (Raphanus sativus) peroxidase in batch process and continuous reactor for the degradation of reactive dyes. Biochem Eng J 46:96–104

Shi L, Zhang X, Chen Z (2011a) Removal of chromium(VI) from wastewater using bentonite-supported nanoscale zero-valent iron. Water Res 45:886–892

Shi L, Lin Y, Zhang X et al (2011b) Synthesis, characterization and kinetics of bentonite supported nZVI for the removal of Cr(VI) from aqueous solution. Chem Eng J 171:612–617

Soliemanzadeh A, Fekri M (2017) The application of green tea extract to prepare bentonite-supported nanoscale zero-valent iron and its performance on removal of Cr(VI): effect of relative parameters and soil experiments. Microporous Mesoporous Mater 239:60–69

Su J, Hao H, Lv X et al (2020) Properties and mechanism of hexavalent chromium removal by FeS@graphite carbon nitride nanocomposites. Colloids Surf A 597:124751

Wan S, Ding W, Wang Y et al (2018) Manganese oxide nanoparticles impregnated graphene oxide aggregates for cadmium and copper remediation. Chem Eng J 350:1135–1143

Wang C, Luo H, Zhang Z et al (2014) Removal of As(III) and As(V) from aqueous solutions using nanoscale zero valent iron-reduced graphite oxide modified composites. J Hazard Mater 268:124–131

Wang K, Sun Y, Tang J et al (2020) Aqueous Cr(VI) removal by a novel ball milled Fe^0-biochar composite: role of biochar electron transfer capacity under high pyrolysis temperature. Chemosphere 241:125044

Wang H, Wang S, Wang S et al (2022) Adenosine-functionalized UiO-66-NH_2 to efficiently remove Pb(II) and Cr(VI) from aqueous solution: thermodynamics, kinetics and isothermal adsorption. J Hazard Mater 425:127771

Wei X, Li X, Tang L et al (2021) Exploring the role of Fe species from biochar-iron composites in the removal and long-term immobilization of SeO_4^{2-} against competing oxyanions. J Hazard Mater 418:126311

Wu H, Li L, Chang K et al (2020) Graphene oxide decorated nanoscale iron sulfide for highly efficient scavenging of hexavalent chromium from aqueous solutions. J Environ Chem Eng 8:103882

Wu H, Chen J, Xu L et al (2021) Decorating nanoscale FeS onto metal-organic framework for the decontamination performance and mechanism of Cr(VI) and Se(IV). Colloids Surf A 625:126887

Xing M, Xu L, Wang J (2016) Mechanism of Co(II) adsorption by zero valent iron/graphene nanocomposite. J Hazard Mater 301:286–296

Xu J, Li Y, Jing C et al (2014) Removal of uranium from aqueous solution using montmorillonite-supported nanoscale zero-valent iron. J Radioanal Nucl Chem 299:329–336

Yao L, Hu Y, Zou Y et al (2022a) Selective and efficient photoextraction of aqueous Cr(VI) as a solid state polyhydroxy Cr(V) complex for environmental remediation, and resource recovery. Environ Sci Technol 56:14030–14037

Yao L, Shen Z, Ji ZZ et al (2022) Cr(VI) detoxification and simultaneous selective recovery of Cr resource from wastewater via photo-chemical extraction using biomass. Sci Bull 67:2154–2157

Zhang Y, Jiang H, Zhang Y et al (2013) The dispersity-dependent interaction between montmorillonite supported nZVI and Cr(VI) in aqueous solution. Chem Eng J 229:412–419

Zhang YC, Yao L, Zhang G et al (2014) One-step hydrothermal synthesis of high-performance visible-light-driven SnS_2/SnO_2 nanoheterojunction photocatalyst for the reduction of aqueous Cr(VI). Appl Catal B: Environ 144:730–738

Zhang F, Zhang Y, Zhang G et al (2018) Exceptional synergistic enhancement of the photocatalytic activity of SnS_2 by coupling with polyaniline and N-doped reduced graphene oxide. Appl Catal B: Environ 236:53–63

Zhang F, Zhang Y, Wang Y et al (2022) Efficient photocatalytic reduction of aqueous Cr (VI) by Zr^{4+} doped and polyaniline coupled SnS_2 nanoflakes. Sep Purif Technol 283:120161

Zhao J, Niu Y, Ren B et al (2018) Synthesis of Schiff base functionalized superparamagnetic Fe_3O_4 composites for effective removal of Pb(II) and Cd(II) from aqueous solution. Chem Eng J 347:574–584